Luttinger liquid on a lattice

Zakharov, V.

Chapter 3

Luttinger liquid tensor network: sine versus tangent dispersion of massless Dirac fermions

3.1 Introduction

The linear energy-momentum relation, $E = \pm\hbar v k$, of massless Dirac fermions remains gapless in the presence of disorder, provided that a pair of fundamental symmetries, chiral symmetry and time reversal symmetry, are not both broken [54]. To preserve this so-called topological protection on a lattice one needs to work around the fermion doubling obstruction [5]: if the Brillouin zone contains multiple Dirac cones they can hybridize and open a gap at $E = 0$. The nearest-neighbor finite difference discretization suffers from this problem: The resulting sine dispersion, $E = (\hbar v/a) \sin ak$, has a spurious second Dirac cone at the edge $k = \pi/a$ of the Brillouin zone.

It was shown recently [45, 17] that an alternative discretization of the differential operator, introduced in the 1980's by Stacey [16], preserves a gapless Dirac cone in a disordered system. The dispersion is a tangent, $E = (2\hbar v/a) \tan(ak/2)$, with a pole rather than a zero at the Brillouin zone edge. No other discretization scheme (staggered fermions, Wilson fermions, SLAC fermions [18]) has this topological protection. One fundamental consequence is that the Casimir effect for lattice fermions requires the tangent discretization [51].

All of this is for non-interacting particles. Interacting models of massless Dirac fermions need a lattice formulation for numerical studies [55, 56, 57, 58], which use methods such as quantum Monte Carlo or DMRG (density matrix renor-

malization group). The Luttinger liquid with Hubbard interaction, a paradigmatic non-Fermi liquid [13, 21], can be solved analytically in the continuum via bosonization [3, 20], providing a testing ground for lattice calculations. Such a test was reported for quantum Monte Carlo in Ref. [59]. Here we consider the DMRG implementation.

The two techniques require a different approach, each with its own challenges. For quantum Monte Carlo the discretization is at the level of the Lagrangian, and the challenge is to ensure a positive action determinant (avoiding the so-called sign problem). For DMRG the discretization involves the representation of the second quantized Hamiltonian by a tensor network [60, 61]: a product of matrices of operators acting locally on each site. The challenge is to ensure that the rank of each matrix (the bond dimension) is small and does not grow with the number of sites.

Tangent fermions have a hidden locality originating from the fact that — although the tangent discretization produces a Hamiltonian with a highly non-local, non-decaying, coupling of distant sites [16] — the ground state can be obtained from a *local* generalized eigenproblem [44]. Our key finding is that this allows for an exact matrix-product-operator (MPO) representation of low bond dimension. In an independent study [52], Haegeman *et al.* reached the same conclusion.

In what follows we will compare the sine and tangent discretizations of the Luttinger Hamiltonian, and test the correlators against the continuum results. We first construct the MPO explicitly in Sec. 3.2. The correlators are calculated via the DMRG approach and compared with bosonization in Sec. 3.3. We conclude in Sec. 3.4. Appendix 3.A contains the connection between a local generalized eigenproblem and a scale-independent MPO.

3.2 Matrix product operator

The starting point of a tensor network DMRG calculation [57] is the representation of the Hamiltonian by a matrix product operator (MPO), to ensure that the variational ground state energy can be computed efficiently for a matrix product state.

In this section we construct the MPO representation of the one-dimensional (1D) Dirac Hamiltonian

$$H = -i\hbar v \begin{pmatrix} \partial/\partial x & 0 \\ 0 & -\partial/\partial x \end{pmatrix}, \tag{3.1}$$

discretized on a lattice. (The matrix structure refers to the spin degree of freedom.) Once we have done that we will compute the correlators via DMRG in the presence of a Hubbard interaction (Luttinger model).

3.2.1 Free fermions

Consider noninteracting, spinless chiral fermions on a chain of N sites (unit spacing), with hopping matrix elements t_{nm} ($n > m \geq 1$). (We will include the spin degree of freedom and the electron-electron interaction later on.) For an infinite translationally invariant lattice, $t_{nm} = t(n-m)$ is a Fourier coefficient of the dispersion relation,

$$E(k) = 2\,\mathrm{Re}\sum_{n=1}^{\infty} t(n)e^{ink}. \tag{3.2}$$

The second quantized Hamiltonian

$$H = \sum_{n>m=1}^{N} \left(t_{nm}c_n^\dagger c_m + t_{nm}^* c_m^\dagger c_n\right) \tag{3.3}$$

can be rewritten as a product of matrices $M^{(n)}$ that act only on site n, but the dimension of each matrix (the bond dimension) will typically grow linearly with N.

An exact MPO representation with scale-independent bond dimension is possible in two cases [62, 63, 64, 65]: for a short-range hopping ($t_{nm} \equiv 0$ for $n - m > r$) and for a long-range hopping with a polynomial-times-exponential distance dependence:

$$t_{nm} = 2t_0 e^{i\phi}(n-m)^p e^{\beta(n-m)}, \quad \beta \in \mathbb{C}, \quad p \in \mathbb{N}, \tag{3.4}$$

and linear combinations of this functional form. While the exponent $\beta = \beta_1 + i\beta_2$ can be an arbitrary complex number, the power p must be a non-negative integer [65]. A decaying $t_{nm} \propto 1/(n-m)^p$ does not qualify.

The sine dispersion corresponds to a short-range, nearest-neighbor hopping,

$$t_{nm} = (t_0/2i)\delta_{n-m,1} \Leftrightarrow E(k) = t_0 \sin k. \tag{3.5}$$

The MPO Hamiltonian has bond dimension 4,

$$H_{\text{sine}} = \tfrac{1}{2} i t_0 [M^{(1)} M^{(2)} \cdots M^{(N)}]_{1,4}, \tag{3.6a}$$

$$M^{(n)} = \begin{pmatrix} 1 & c_n & c_n^\dagger & 0 \\ 0 & 0 & 0 & c_n^\dagger \\ 0 & 0 & 0 & c_n \\ 0 & 0 & 0 & 1 \end{pmatrix}. \tag{3.6b}$$

A no-go theorem [5] forbids short-range hopping if one wishes to avoid fermion doubling and preserve chiral symmetry. If we also require a scale-independent bond dimension we need the hopping (3.4). In the simplest case $p = 0$ of a purely exponential distance dependence[1], one has the dispersion

$$E(k) = 2t_0 \frac{e^{\beta_1} \cos\phi - \cos(\beta_2 + k + \phi)}{\cos(\beta_2 + k) - \cosh\beta_1}. \tag{3.7}$$

This should be a continuous function in the interval $(-\pi, \pi)$, crossing $E = 0$ at $k = 0$ but not at any other point in this interval. The only parameter choice consistent with these requirements is $\phi = \pi/2$, $\beta_1 = 0$, $\beta_2 = \pi$, when

$$t_{nm} = 2it_0(-1)^{n-m} \Leftrightarrow E(k) = 2t_0 \tan(k/2). \tag{3.8}$$

This is Stacey's tangent dispersion[2] [16].

The corresponding MPO Hamiltonian is

$$H_{\text{tangent}} = 2it_0 [M^{(1)} M^{(2)} \cdots M^{(N)}]_{1,4}, \tag{3.9a}$$

$$M^{(n)} = \begin{pmatrix} 1 & c_n & c_n^\dagger & 0 \\ 0 & -1 & 0 & c_n^\dagger \\ 0 & 0 & -1 & c_n \\ 0 & 0 & 0 & 1 \end{pmatrix}, \tag{3.9b}$$

again with bond dimension 4, differing from the sine MPO (3.6) by the -1's on the diagonal.

[1] The tangent discretization (3.8) corresponds to Eq. (3.4) with $p = 0$ (purely exponential distance dependence). More generally, one can take $p = 1, 2, \ldots$ (polynomial-times-exponential distance dependence), in which case the dispersion contains terms $\propto \tan(k/2)(1 + \cos k)^{-p}$. The MPO representation of the discretized Hamiltonian remains scale independent, but the bond dimension is larger than for $p = 0$.

[2] The Fourier series $\tan(k/2) = -2\sum_{n=1}^{\infty}(-1)^n \sin nk$ implied by the identification (3.8) should be understood in the sense of a distribution: $\int_0^\pi \tan(k/2) f(k)\, dk = -2\sum_{n=1}^{\infty}(-1)^n \int_0^\pi f(k) \sin nk\, dk$, with $f(k)$ a test function that vanishes at π.

3.2.2 Helical Luttinger liquid

We next include the spin degree of freedom and consider helical instead of chiral fermions,

$$H = \sum_{n>m=1}^{N} \Big[t_{nm} \big(c^\dagger_{n\uparrow} c_{m\uparrow} - c^\dagger_{n\downarrow} c_{m\downarrow} \big) + \text{H.c.} \Big] + \sum_{n=1}^{N} U_n. \tag{3.10}$$

(H.c. denotes the Hermitian conjugate.) We have added an on-site Hubbard interaction,

$$U_i = U(n_{i\uparrow} - \tfrac{1}{2})(n_{i\downarrow} - \tfrac{1}{2}), \quad n_{i\sigma} = c^\dagger_{i\sigma} c_{i\sigma}. \tag{3.11}$$

The MPO representation for the tangent discretization (3.8) is

$$H_{\text{tangent}} = 2it_0 [M^{(1)} M^{(2)} \cdots M^{(N)}]_{1,6}, \tag{3.12a}$$

$$M^{(n)} = \begin{pmatrix} 1 & c_{n\uparrow} & c^\dagger_{n\uparrow} & c_{n\downarrow} & c^\dagger_{n\downarrow} & (2it_0)^{-1} U_n \\ 0 & -1 & 0 & 0 & 0 & c^\dagger_{n\uparrow} \\ 0 & 0 & -1 & 0 & 0 & c_{n\uparrow} \\ 0 & 0 & 0 & -1 & 0 & -c^\dagger_{n\downarrow} \\ 0 & 0 & 0 & 0 & -1 & -c_{n\downarrow} \\ 0 & 0 & 0 & 0 & 0 & 1 \end{pmatrix}, \tag{3.12b}$$

with bond dimension 6. For the sine discretization the -1's on the diagonal are replaced by 0's,

$$H_{\text{sine}} = \tfrac{1}{2} it_0 [M^{(1)} M^{(2)} \cdots M^{(N)}]_{1,6}, \tag{3.13a}$$

$$M^{(n)} = \begin{pmatrix} 1 & c_{n\uparrow} & c^\dagger_{n\uparrow} & c_{n\downarrow} & c^\dagger_{n\downarrow} & (\frac{1}{2} it_0)^{-1} U_n \\ 0 & 0 & 0 & 0 & 0 & c^\dagger_{n\uparrow} \\ 0 & 0 & 0 & 0 & 0 & c_{n\uparrow} \\ 0 & 0 & 0 & 0 & 0 & -c^\dagger_{n\downarrow} \\ 0 & 0 & 0 & 0 & 0 & -c_{n\downarrow} \\ 0 & 0 & 0 & 0 & 0 & 1 \end{pmatrix}. \tag{3.13b}$$

To deal with fermionic statistics, we apply the Jordan-Wigner transformation to the MPOs (see App. 3.B).

The MPOs written down so far refer to an open chain of N sites. To minimize finite-size effects periodic boundary conditions are preferrable: the chain is wrapped around a circle, and sites n and $n + N$ are identified. A translationally invariant hopping, $t_{nm} = t(n - m)$, then requires

$$t(N - n) = t(n)^*, \quad 1 \le n \le N - 1. \tag{3.14}$$

For N odd the Hamiltonian in the tangent discretization (3.8) satisfies this condition without further modification: because of the all-to-all hopping a closing of the chain on a circle makes no difference. (For N even one would have antiperiodic boundary conditions[3].) We can therefore still use the MPO (3.12).

The sine discretization (3.5) requires an additional hopping term between sites 1 and N. We construct this MPO explicitly in App. 3.C.

3.3 Correlators

3.3.1 Free fermions

The propagator

$$C_\sigma(x,x') = \langle c^\dagger_\sigma(x) c_\sigma(x')\rangle, \quad \sigma \in \{\uparrow,\downarrow\} \leftrightarrow \{1,-1\}, \tag{3.15}$$

of a non-interacting 1D Dirac fermion with dispersion $E(k) = \pm\hbar v k$ can be readily evaluated:

$$\begin{aligned} C_\sigma(x,x') = \frac{1}{Z}\operatorname{Tr} e^{-\beta H} c^\dagger_\sigma(x) c_\sigma(x') &= \int_{-\infty}^{\infty} \frac{dk}{2\pi} \frac{e^{ik(x-x')}}{1+e^{\beta E(k)}} \\ &= \frac{\sigma\hbar v}{2i\beta \sinh[\pi(\hbar v/\beta)(x-x')]}, \end{aligned} \tag{3.16}$$

for $x \neq x'$, with $Z = \operatorname{Tr} e^{-\beta H}$ the partition function at inverse temperature $\beta = 1/k_\mathrm{B}T$. This reduces to

$$\lim_{\beta\to\infty} C_\sigma(x,x') = \frac{\sigma}{2\pi i(x-x')} \tag{3.17}$$

in the zero-temperature limit.

On a lattice ($x/a = n \in \mathbb{Z}$, $c_\sigma(x = na) \equiv c_\sigma(n)$) the integration range of k is restricted to the interval $(-\pi/a, \pi/a)$. In the zero-temperature limit, with $\sigma E(k) < 0$ for $-\pi/a < k < 0$, one then finds

$$C_\sigma(n,m) = \sigma \int_{-\pi/a}^{0} \frac{dk}{2\pi} e^{ika(n-m)} = \begin{cases} \frac{2\sigma}{2\pi i a(n-m)} & \text{if } n-m \text{ is odd,} \\ 0 & \text{if } n-m \text{ is even,} \end{cases} \tag{3.18}$$

[3] As a consistency check, we note that in real space the fact that an odd (even) number N of lattice sites corresponds to periodic (antiperiodic) boundary conditions, ensures in momentum space that the discrete wave numbers avoid the pole of the tangent dispersion relation at the Brillouin zone boundary.

irrespective of the functional form of the dispersion relation $E(k)$. The continuum result (3.17) is only recovered if one averages over even and odd lattice sites.

The even-odd oscillation also appears in the transverse spin correlator,

$$R(x,x') = \tfrac{1}{4}\langle \boldsymbol{c}^\dagger(x)\sigma_x \boldsymbol{c}(x) \;\; \boldsymbol{c}^\dagger(x')\sigma_x \boldsymbol{c}(x')\rangle, \tag{3.19}$$

defined in terms of the spinor $\boldsymbol{c} = (c_\uparrow, c_\downarrow)$ and Pauli matrix σ_x.

For free fermions Wick's theorem gives

$$R(x,x') = -\frac{1}{4}\Big(C_\uparrow(x,x')C_\downarrow(x',x) + C_\downarrow(x,x')C_\uparrow(x',x)\Big), \tag{3.20}$$

which at zero temperature results in

$$R(x,x') = \frac{1}{2}\,[2\pi(x-x')]^{-2}, \tag{3.21}$$

in the continuum and

$$R(n,m) = \begin{cases} 2[2\pi a(n-m)]^{-2} & \text{if } \; n-m \;\text{ is odd,} \\ 0 & \text{if } \; n-m \;\text{ is even.} \end{cases} \tag{3.22}$$

The even-odd oscillation [15] can be removed in a path integral formulation, by discretizing the Lagrangian in both space and (imaginary) time [59], but in the Hamiltonian formulation considered here it is unavoidable. In what follows we will consider smoothed lattice correlators, defined by averaging the fermionic operators $c_\sigma(n)$ over nearby lattice sites. The precise form of the smoothing profile will not matter in the continuum limit $a \to 0$, we take the simple form

$$\bar{c}_{n\sigma} = \tfrac{1}{2}c_{n\sigma} + \tfrac{1}{2}c_{n+1\sigma}, \tag{3.23}$$

so an equal-weight average over adjacent sites. The smoothed correlators are then defined by

$$\bar{C}_\sigma(n,m) = \langle \bar{c}^\dagger_{n\sigma}\bar{c}_{m\sigma}\rangle, \tag{3.24a}$$

$$\bar{R}(n,m) = \tfrac{1}{4}\langle \bar{\boldsymbol{c}}^\dagger_n\sigma_x\bar{\boldsymbol{c}}_n \;\; \bar{\boldsymbol{c}}^\dagger_m\sigma_x\bar{\boldsymbol{c}}_m\rangle. \tag{3.24b}$$

3.3.2 DMRG calculation with Hubbard interaction

We represent the ground state wave function Ψ of the Luttinger liquid Hamiltonian (3.10) by a matrix product state (MPS) and carry out the tensor network DMRG algorithm [57] to variationally minimize $\langle\Psi|H|\Psi\rangle/\langle\Psi|\Psi\rangle$. (We used the TeNPy

Library [66] for these calculations.) We compare the results for tangent and sine discretization. The MPOs for both are exact with small bond dimension (given explicitly in App. 3.B and App. 3.C). The bond dimension χ of the MPS is increased until convergence is reached (see App. 3.D).

The Luttinger liquid is simulated at zero temperature ($\beta \to \infty$) and at fixed particle number $\mathcal{N} = \mathcal{N}_\uparrow + \mathcal{N}_\downarrow$ (canonical ensemble). We take $N = 51$ an odd integer, with periodic boundary conditions for the MPO. The periodicity of the MPS is not prescribed *a priori*, to simplify the DMRG code. By setting $\mathcal{N}_\uparrow = (N+1)/2$ and $\mathcal{N}_\downarrow = (N-1)/2$ we model a half-filled band.

The bosonization theory of an infinite Luttinger liquid gives a power law decay of the zero-temperature, zero-chemical-potential correlators [13],

$$C_\sigma(x,x') \propto |x-x'|^{-(1/2)(K+1/K)}, \tag{3.25a}$$

$$R(x,x') \propto |x-x'|^{-2K}, \tag{3.25b}$$

$$K = \sqrt{(1-\kappa)/(1+\kappa)}, \quad \kappa = \frac{U}{2\pi t_0} \in (-1,1). \tag{3.25c}$$

For repulsive interactions, $U > 0 \Rightarrow K < 1$, the transverse spin correlator R decays more slowly than the $1/x^2$ decay expected from a Fermi liquid.

The numerical results are shown in Figs. 3.1 and 3.2 (data points). The curves are the continuum bosonization formulas (including finite-size corrections, see App. 3.E). The lattice calculations with the tangent dispersion (crosses) agree nicely with the continuum formulas, without any adjustable parameter. The sine dispersion (plusses), in contrast, only agrees for free fermions. With interactions the sine dispersion gives an exponential decay of the propagator, indicative of the opening of an excitation gap.

3.4 Conclusion

We have constructed a Hamiltonian-based tensor network formulation of a Luttinger liquid on a 1D lattice, complementing the Lagrangian-based path integral formulation of Ref. [59]. The key step is the Hermitian discretization of the momentum operator $-i\hbar d/dx$ in a way that preserves the fundamental symmetries (chiral symmetry and time reversal symmetry) of massless Dirac fermions. We have compared two discretizations, both allowing for a tensor network of low, scale-independent bond dimension. In this concluding section we also discuss a third.

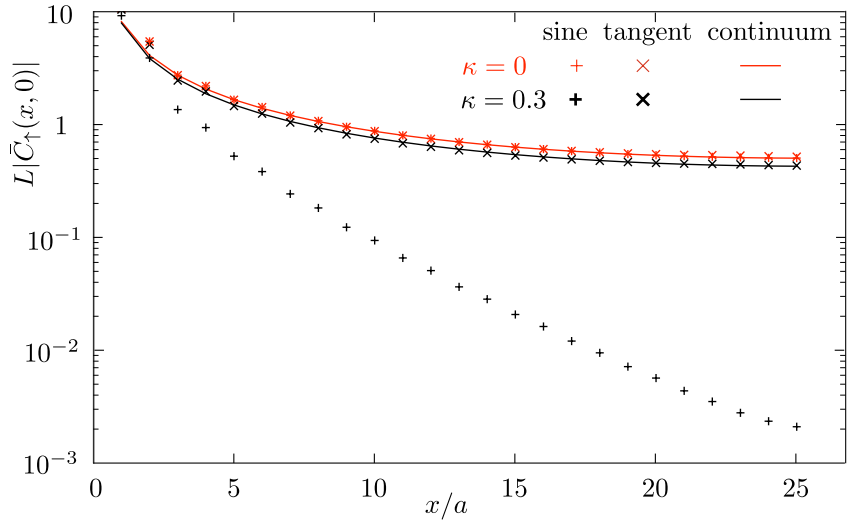

Figure 3.1. Data points: absolute value of the propagator $\bar{C}_\sigma(n,m)$, defined in Eq. (3.24a) for $\sigma = \uparrow$, $n = x/a$ and $m = 0$, calculated in the tensor network of $L/a = 51$ sites and bond dimension $\chi = 4096$ of the matrix-product state. Results are shown for the tangent and sine discretization of the Luttinger Hamiltonian, for free fermions and for a repulsive Hubbard interaction of strength $\kappa = U/2\pi t_0 = 0.3$. The curves are the analytical results in the continuum.

The three discretizations of the differential operator on a 1D lattice (unit lattice constant a) are the following:

$$\frac{df}{dx} \mapsto \tfrac{1}{2}[f(x+1) - f(x-1)] \quad \text{(sine dispersion)}, \tag{3.26a}$$

$$\frac{df}{dx} \mapsto 2\sum_{n=1}^{\infty}(-1)^n[f(x-n) - f(x+n)] \quad \text{(tangent dispersion)}, \tag{3.26b}$$

$$\frac{df}{dx} \mapsto \sum_{n=1}^{\infty}(-1)^n\frac{1}{n}[f(x-n) - f(x+n)] \quad \text{(sawtooth dispersion)}. \tag{3.26c}$$

The corresponding dispersion relations are shown in Fig. 3.3. The energy-momentum relation is a *sine* for the nearest-neighbor difference and a *tangent* for the long-range Stacey derivative [16]. The third dispersion is a (piecewise linear) *sawtooth*, produced by a nonlocal discretization known as the SLAC derivative in

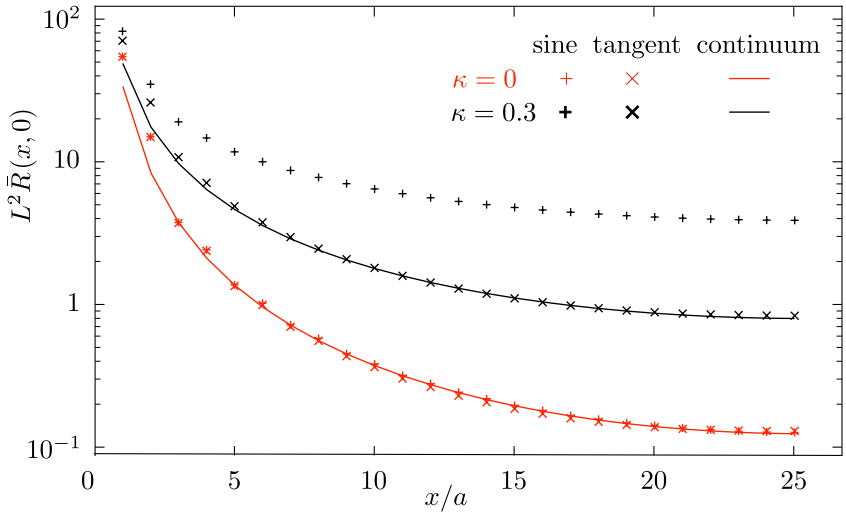

Figure 3.2. Same as Fig. 3.1, but now for the transverse spin correlator $\bar{R}(n,m)$ defined in Eq. (3.24b).

the particle physics literature [35].

The sine dispersion suffers from fermion doubling [18] — a second species of low-energy excitations appears at the Brillouin zone boundary. The tangent and sawtooth dispersion describe an unpaired chiral fermion, they rely on nonlocality to work around the theorem [5] that requires chiral fermions to come in pairs in any local theory on a lattice.

Both the Stacey derivative and the SLAC derivative couple arbitarily distant sites n, m, the former $\propto (-1)^{n-m}$ and the latter $\propto (-1)^{n-m} \times (n-m)^{-1}$. From the perspective of a tensor network there is an essential difference between the two: Because the MPO condition (3.4) allows for an exponential distance dependence but excludes a coupling that decays as a power law with distance, only the tangent dispersion has an exact MPO representation with scale-independent bond dimension — the sawtooth dispersion does not. Tangent fermions have a hidden locality, their spectrum is governed by a *local* generalized eigenproblem [44], which is at the origin of the efficient tensor network (see App. 3.A).

The method we developed here enables simulations of systems with various filling factors and scalar potentials, including those with disorder. By focusing on the impurity-free Luttinger liquid we could in this work test the numerical approach against analytical formulas. The close agreement gives us confidence that tangent fermion DMRG is a reliable method, which at least in 1D is highly

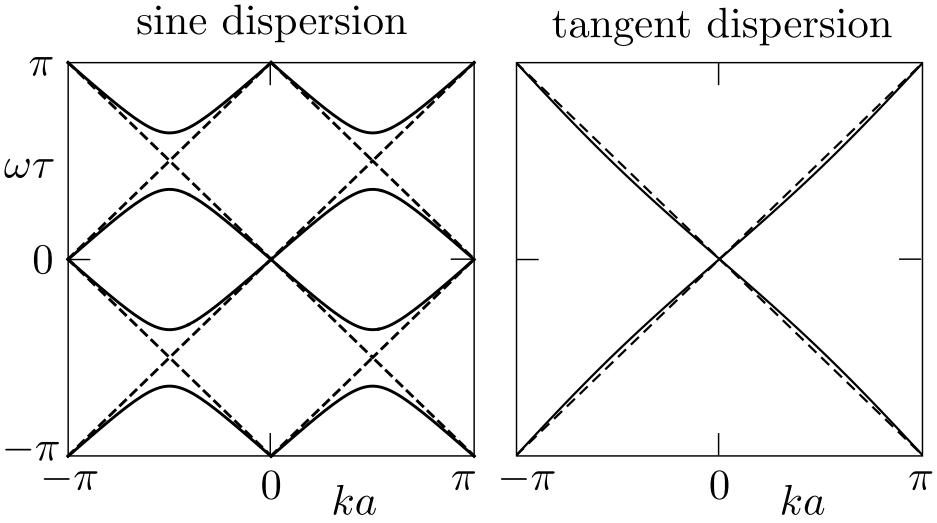

Figure 3.3. The three ways to discretize the derivative operator in Eq. (3.26) produce three different dispersion relations: sine (blue), tangent (red), and sawtooth (black). The energy-momentum relation of a chiral fermion is obtained from the discretized derivative by substituting $f(x+na) = e^{inka} f(x)$ and equating $-i\hbar v df/dx = Ef$. The tangent and sawtooth dispersions are discontinuous at the Brillouin zone boundaries ($k = \pm\pi/a$), where the sine dispersion has a second root (fermion doubling). The three dispersion relations coincide near $k = 0$, so the corresponding discretized derivatives are equivalent if applied to functions that vary smoothly on the scale of the lattice spacing.

efficient.

The next step is to apply it to problems where no analytics exists, condensed matter and particle physics provide a variety of such problems. One class of applications is the stability of gapless chiral modes to the combination of disorder and interactions. Existing DMRG studies [67] work around the fermion doubling obstruction by studying a strip geometry with two edges — tangent fermions would allow for a single-edge implementation.

For such applications it would of interest to proceed from 1D to 2D. It is known that in two spatial dimensions the tangent discretization of $\sigma_x df/dx + \sigma_y df/dy$ still allows for a reformulation of $\mathcal{H}\psi = E\psi$ as a generalized eigenvalue problem [44]:

$$\begin{aligned} &Q\psi = E\mathcal{P}\psi, \quad \mathcal{P} = \tfrac{1}{4}(1+\cos k_x)(1+\cos k_y), \\ &Q = \tfrac{1}{2}\sigma_x(1+\cos k_y)\sin k_x + \tfrac{1}{2}\sigma_y(1+\cos k_x)\sin k_y. \end{aligned} \tag{3.27}$$

Therefore, we expect that an efficient 2D tensor network representation of the 2D

tangent Hamiltonian in the form of Projected Entangled Pair Operators (PEPO) [58] can be constructed similarly to the 1D MPO approach.

Appendices

3.A Local generalized eigenproblem allows for a scale-independent MPO

The DMRG approach described in the main text works because the tangent fermion Hamiltonian, while having a highly nonlocal long-range coupling, can still be described by an MPO with a low and scale-independent bond dimension. Ref. [44] attributes the "hidden locality" of tangent fermions to the fact that their spectrum is obtained from a *local* generalized eigenproblem. Here we make the connection to the scale-independent MPO explicit.

Consider 1D lattice fermions with a dispersion relation $E(k) = P(k)/Q(k)$ such that both $P(k)$ and $Q(k)$ are polynomials of finite degree in e^{ik},

$$P(k) = \sum_{n=0}^{N_P} p_n e^{ink}, \quad Q(k) = \sum_{n=0}^{N_Q} q_n e^{ink}. \tag{3.28}$$

For example, the tangent dispersion $E(k) = 2\tan(k/2)$ corresponds to $P(k) = 2i(1 - e^{ik})$, $Q(k) = 1 + e^{ik}$. In real space the operators P and Q couple sites separated by at most N_P or N_Q lattice spacings. The generalized eigenproblem $P\Psi = EQ\Psi$ is therefore local.

Consider first the case that

$$Q(k) = \prod_{n=1}^{N_Q} (\alpha_n - e^{ik}) \tag{3.29}$$

has *distinct* roots α_n. The partial fraction decomposition is

$$\frac{P(k)}{Q(k)} = D(k) + \sum_{n=1}^{N_Q} \frac{\beta_n}{\alpha_n - e^{ik}} \tag{3.30}$$

with $D(k)$ a polynomial of degree $N_P - N_Q$ (vanishing if $N_P < N_Q$). The sum over n corresponds in real space to a sum over coupling terms t_{ij} with an exponential spacing dependence $\propto (1/\alpha_n)^{i-j}$ for $i > j$. So in this case of distinct roots we are guaranteed to have an exact MPO representation with scale-independent bond dimension.

The situation is slightly more complicated if $Q(k)$ has repeated roots,

$$Q(k) = \prod_{n=1}^{L} (\alpha_n - e^{ik})^{\ell_n}, \quad \sum_{n=1}^{L} \ell_n = N_Q. \tag{3.31}$$

The partial fraction decomposition now reads

$$\frac{P(k)}{Q(k)} = D(k) + \sum_{n=1}^{L} \sum_{m=1}^{\ell_n} \frac{\beta_{nm}}{(\alpha_n - e^{ik})^m}. \tag{3.32}$$

A term $1/(\alpha_n - e^{ik})^m$ corresponds in real space to a coupling $t_{ij} \propto (1/\alpha_n)^{i-j} \times Z(i-j)$ that is an exponential times a polynomial Z in the spacing of degree $m-1$. This is still of the form (3.4) that allows for a scale-independent MPO [65].

3.B Jordan-Wigner transformation

To enable the DMRG calculation, we need to convert the fermionic operators $c_{n\sigma}$ into bosonic operators $a_{n\sigma}$ (hard-core bosons, excluding double occupancy of a state). This is achieved by the Jordan-Wigner transformation,

$$\begin{aligned} c_{n\uparrow} &= F_1 F_2 \cdots F_{n-1} a_{n\uparrow}, \\ c_{n\downarrow} &= F_1 F_2 \cdots F_{n-1} F_n a_{n\downarrow}, \end{aligned} \tag{3.33}$$

with fermion parity operator

$$F_i = (1 - 2n_{i\uparrow})(1 - 2n_{i\downarrow}) = (-1)^{n_{i\uparrow} + n_{i\downarrow}}. \tag{3.34}$$

The transformation does not increase the bond dimension of the MPO, instead of Eq. (3.12) one now has

$$H_{\text{tangent}} = 2it_0 [M^{(1)} M^{(2)} \cdots M^{(N)}]_{1,6}, \tag{3.35a}$$

$$M^{(n)} = \begin{pmatrix} 1 & a_{n\uparrow} F_n & a^\dagger_{n\uparrow} F_n & a_{n\downarrow} & a^\dagger_{n\downarrow} & (2it_0)^{-1} U_n \\ 0 & -F_n & 0 & 0 & 0 & a^\dagger_{n\uparrow} \\ 0 & 0 & -F_n & 0 & 0 & a_{n\uparrow} \\ 0 & 0 & 0 & -F_n & 0 & -F_n a^\dagger_{n\downarrow} \\ 0 & 0 & 0 & 0 & -F_n & -F_n a_{n\downarrow} \\ 0 & 0 & 0 & 0 & 0 & 1 \end{pmatrix}. \tag{3.35b}$$

This is for the tangent discretization. For the sine discretization the $-F_n$ on the diagonal are replaced by 0,

$$H_{\text{sine}} = \tfrac{1}{2} i t_0 [M^{(1)} M^{(2)} \cdots M^{(N)}]_{1,6}, \tag{3.36a}$$

$$M^{(n)} = \begin{pmatrix} 1 & a_{n\uparrow} F_n & a^\dagger_{n\uparrow} F_n & a_{n\downarrow} & a^\dagger_{n\downarrow} & (\tfrac{1}{2} i t_0)^{-1} U_n \\ 0 & 0 & 0 & 0 & 0 & a^\dagger_{n\uparrow} \\ 0 & 0 & 0 & 0 & 0 & a_{n\uparrow} \\ 0 & 0 & 0 & 0 & 0 & -F_n a^\dagger_{n\downarrow} \\ 0 & 0 & 0 & 0 & 0 & -F_n a_{n\downarrow} \\ 0 & 0 & 0 & 0 & 0 & 1 \end{pmatrix}. \tag{3.36b}$$

3.C Periodic boundary condition for MPO with sine discretization

The sine discretization (3.5) requires an additional hopping term between sites 1 and N. The modified MPO has bond dimension 10,

$$H_{\text{sine}} = \tfrac{1}{2} i t_0 [\tilde{M}^{(1)} \tilde{M}^{(2)} \cdots \tilde{M}^{(N)}]_{1,6}, \tag{3.37a}$$

$$\tilde{M}^{(n)} = \begin{pmatrix} M^{(n)} & \delta_{n,1} W^{(n)} \\ \delta_{n,N} W^{(n)} & (1 - \delta_{n,1} - \delta_{n,N}) W^{(n)} \end{pmatrix}, \tag{3.37b}$$

with $M^{(n)}$ as in Eq. (3.36) and

$$W^{(1)} = \begin{pmatrix} a_{1\uparrow} F_1 & a^\dagger_{1\uparrow} F_1 & a_{1\downarrow} & a^\dagger_{1\downarrow} \\ 0 & 0 & 0 & 0 \\ 0 & 0 & 0 & 0 \\ 0 & 0 & 0 & 0 \\ 0 & 0 & 0 & 0 \end{pmatrix}, \tag{3.37c}$$

$$W^{(1<n<N)} = \begin{pmatrix} F_n & 0 & 0 & 0 \\ 0 & F_n & 0 & 0 \\ 0 & 0 & F_n & 0 \\ 0 & 0 & 0 & F_n \end{pmatrix}, \tag{3.37d}$$

$$W^{(N)} = \begin{pmatrix} 0 & 0 & 0 & 0 & 0 & a^\dagger_{N\uparrow} \\ 0 & 0 & 0 & 0 & 0 & a_{N\uparrow} \\ 0 & 0 & 0 & 0 & 0 & -F_N a^\dagger_{N\downarrow} \\ 0 & 0 & 0 & 0 & 0 & -F_N a_{N\downarrow} \end{pmatrix} \tag{3.37e}$$

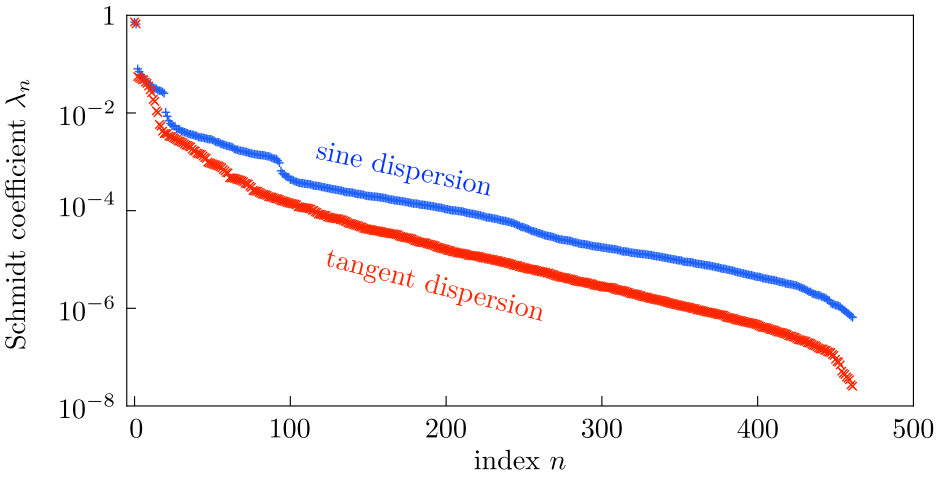

Figure 3.4. Log-linear plot of the Schmidt coefficients λ_n of the ground state wave function of the Luttinger liquid Hamiltonian (3.10) ($U = t_0$, $N = 11$ partitioned into $N_1 = 5$ and $N_2 = 6$), for the sine and tangent dispersions (3.5) and (3.8). The exponential decay allows for an MPS with bond dimension $\chi \ll 4^{N/2}$.

3.D Convergence of the DMRG calculations

The tensor network formulation of the Luttinger liquid on an N-site chain is based on two matrix-product representations: of the operator H (MPO) and of the state Ψ (MPS). The MPO is exact, in terms of an N-fold product of 6×6 matrices of creation and annihilation operators.

The MPS is approximate: defined on N sites with physical dimensional d, it is an N-fold product of $\chi \times \chi \times d$ tensors that introduces an error of order $N \sum_{n>\chi} \lambda_n^2$, with $1 \geq \lambda_1 \geq \lambda_2 \geq \cdots \geq \lambda_{d^{N/2}} \geq 0$ the coefficients in the Schmidt decomposition of $\Psi \in \mathcal{H}_1 \otimes \mathcal{H}_2$ (describing the entanglement between the first and second half of the chain, with Hilbert spaces $\mathcal{H}_1$ and $\mathcal{H}_2$) [68].

The MPS is efficient at bond dimension $\chi \ll d^{N/2}$ if the Schmidt coefficients λ_n decrease exponentially with n. In Fig. 3.4 we check this for both the sine and tangent dispersions. In Fig. 3.5 we show the convergence of the DMRG calculation with increasing χ. We conclude that $\chi = 4^6 \ll 4^{25}$ (in our case $d = 4$) is sufficient for the results to converge to the expected behavior.

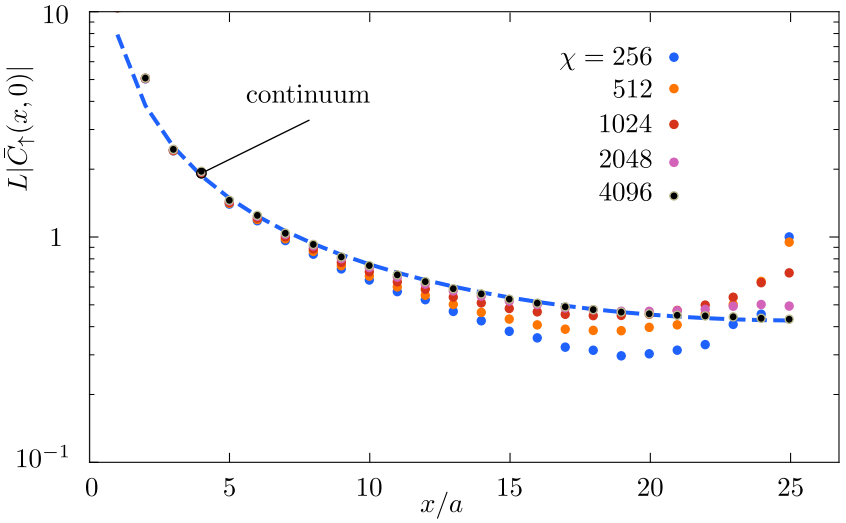

Figure 3.5. Dependence of the propagator on the bond dimension χ of the MPS in the tangent fermion Luttinger liquid ($L/a = 51$, $\kappa = 0.3$). The data in Fig. 3.1 (black crosses) corresponds to $\chi = 4096$.

3.E Bosonization results with finite-size effects

The power law correlators (3.25) follow from bosonization of the helical Luttinger liquid in the limit of an infinite system [13]. To reliably compare with the numerical results on a lattice of length L we need to include finite size effects [14]. In Ref. [59] such a calculation was reported for the grand canonical ensemble (fixed chemical potential) at finite temperature, appropriate for quantum Monte Carlo. For the DMRG calculations we need the results at zero temperature in the canonical ensemble (fixed particle number $\mathcal{N} = \mathcal{N}_\uparrow + \mathcal{N}_\downarrow$).

The Hamiltonian of a helical Luttinger liquid with Hubbard interaction on a ring of length L (periodic boundary conditions) is given by

$$H = \int_{-L/2}^{L/2} dx \Big(v\psi_\uparrow^\dagger(x) p_x \psi_\uparrow(x) - v\psi_\downarrow^\dagger(x) p_x \psi_\downarrow(x) + Ua\rho_\uparrow(x)\rho_\downarrow(x) \Big). \quad (3.38)$$

The density $\rho_\sigma =: \psi_\sigma^\dagger \psi_\sigma :$ is normal ordered — the Fermi sea of a half-filled band (N particles) is subtracted.

The bosonization results in the canonical ensemble at zero temperature are

[59]

$$C_\sigma(x,0) = \frac{\sigma e^{i\pi(2\mathcal{N}_\sigma - N)x/L}}{2\pi i a_* |(L/\pi a_*)\sin(\pi x/L)|^{(1/2)(K+1/K)}}, \tag{3.39a}$$

$$R(x,0) = \frac{\cos\big(2\pi(\mathcal{N}-N)x/L\big)}{2(2\pi a_*)^2 |(L/\pi a_*)\sin(\pi x/L)|^{2K}}, \tag{3.39b}$$

$$K = \sqrt{(1-\kappa)/(1+\kappa)}, \quad \kappa = \frac{U}{2\pi t_0} \in (-1,1). \tag{3.39c}$$

The hopping energy is t_0 and a_* is a short-distance (UV) regularization constant. For the comparison with a lattice calculation we identify $t_0 = \hbar v/a$ and take $L/a = N$ an odd integer. The half-filled band corresponds to $\mathcal{N}_\sigma = (N+\sigma)/2$. To relate the lattice constant a to the continuum regularization constant a_* we argue as follows.

In the continuum theory [14] large momentum transfers q are cut-off by the substitution

$$c^\dagger_{\sigma,q/2} c_{-q/2} \mapsto e^{-qa_*/2} c^\dagger_{\sigma,q/2} c_{-q/2}. \tag{3.40}$$

On the lattice the averaging (3.23) takes care of the UV regularization,

$$\begin{aligned} &c^\dagger_{\sigma,q/2} c_{-q/2} \mapsto \bar{c}^\dagger_{\sigma,q/2} \bar{c}_{\sigma,-q/2} = f(q) c^\dagger_{\sigma,q/2} c_{\sigma,-q/2}, \\ &f(q) = \tfrac{1}{4}(1+e^{-iqa/2})^2, \quad |f(q)| = \cos^2(qa/4). \end{aligned} \tag{3.41}$$

We fix the ratio a/a_* by equating the integrated weight factors,

$$\int_0^{2\pi/a} e^{-qa_*/2}\, dq = \int_0^{2\pi/a} |f(q)|\, dq \Rightarrow a/a_* \approx 2. \tag{3.42}$$

The resulting correlators are plotted in Figs. 3.1 and 3.2.

3.F Alternative tensor network representation of Ref. [52]

An alternative tensor network representation of the problem has been developed in Ref. [52], starting from the transformations

$$\boldsymbol{a} = D^\dagger \boldsymbol{c}, \quad \boldsymbol{b} = D^{-1}\boldsymbol{c}, \quad D_{nm} = \tfrac{1}{2}(\delta_{n,m} + \delta_{n,m-1}), \tag{3.43}$$

of the free fermion operators c_n. These are not canonical transformations, as a consequence the commutation relations of the a- and b-operators are nontrivial:

$$\begin{aligned} &\{a_n, a^\dagger_m\} = (D^\dagger D)_{nm}, \ \{b_n, b^\dagger_m\} = (D^\dagger D)^{-1}_{nm}, \\ &\{c_n, c^\dagger_m\} = \delta_{nm}, \quad \{b_n, a^\dagger_m\} = \delta_{nm}. \end{aligned} \tag{3.44}$$

The corresponding N-fermion bases in Fock space are

$$\begin{aligned} |\psi\rangle &= \sum_{n_i=0,1} \psi^{\alpha}_{n_1,\ldots,n_N} |n_1,\ldots,n_N\rangle_\alpha, \\ |n_1,\ldots,n_N\rangle_\alpha &= (\alpha_1^\dagger)^{n_1}\ldots(\alpha_N^\dagger)^{n_N}, \end{aligned} \tag{3.45}$$

with $\alpha \in \{a, b, c\}$. Only the c-basis is orthonormal, the two other bases produce non-diagonal norm matrices $\tilde{N}$,

$$\begin{aligned} {}_a\langle m_1,\ldots,m_N|n_1,\ldots,n_N\rangle_a &= \tilde{N}^{m_1,\ldots,m_N}_{n_1,\ldots,n_N}, \\ {}_b\langle m_1,\ldots,m_N|n_1,\ldots,n_N\rangle_b &= (\tilde{N}^{-1})^{m_1,\ldots,m_N}_{n_1,\ldots,n_N}, \\ {}_c\langle m_1,\ldots,m_N|n_1,\ldots,n_N\rangle_c &= \delta_{m_1 n_1}\cdots\delta_{m_N n_N}. \end{aligned} \tag{3.46}$$

The a and b bases are bi-orthogonal,

$${}_a\langle m_1,\ldots,m_N|n_1,\ldots,n_N\rangle_b = \delta_{m_1 n_1}\cdots\delta_{m_N n_N}. \tag{3.47}$$

The motivation for these transformations is that the tangent fermion Hamiltonian becomes local in terms of the b-operators,

$$H_{\text{tangent}} = 2it_0 \sum_{n>m=1}^{N} (-1)^{n-m}\left(c_n^\dagger c_m - c_m^\dagger c_n\right) \tag{3.48a}$$

$$= \frac{t_0}{2i}\sum_{n=1}^{N}\left(b_{n+1}^\dagger b_n - b_n^\dagger b_{n+1}\right). \tag{3.48b}$$

Matrix elements of H_{tangent} in the a-basis, orthogonal to the b-basis, can therefore be evaluated efficiently.

The key step of Ref. [52] is to derive a scale-independent MPO representation of the norm matrix $\tilde{N}$ in the a-basis. We have followed a different route, we stay with the orthonormal c-basis and a nonlocal Hamiltonian, but we have found that it does not stand in the way of a scale-independent MPO representation.

Chapter 4

Majorana-metal transition in a disordered superconductor: percolation in a landscape of topological domain walls

4.1 Introduction

While a superconductor is a perfect conductor of electricity, it generally conducts heat poorly. Adding disorder is not expected to improve this, but in a two-dimensional (2D) superconductor with chiral p-wave pairing [69] the unexpected happens: If sufficiently many defects are added the thermal insulator becomes a thermal metal [70, 71, 72]. This unusual state is known as a Majorana metal, because the quasiparticles that conduct the heat are Majorana fermions (equal-weight superpositions of electrons and holes). Although the transition from a thermal insulator to a thermal metal has not yet been observed in experiments, it has been demonstrated in computer simulations [73, 74, 75, 76, 77, 78, 79, 80].

The Majorana-metal transition is well understood if the defects consist of the Abrikosov vortices that appear when a perpendicular magnetic field is applied to a type-II superconductor. A vortex can bind sub-gap quasiparticles [81], but bound states in nearby vortices will not typically be aligned in energy, making them inefficient for heat transport. A special property of a chiral p-wave superconductor is that its vortices have a bound state exactly in the middle of the gap ($E = 0$, the Fermi level), a socalled Majorana zero-mode [82, 83, 84, 85, 86]. The energetic

alignment of Majorana zero-modes allows for resonant heat conduction when the density of Abrikosov vortices crosses a critical threshold [73, 74].

Electrostatic disorder in zero magnetic field can also produce a thermal metal phase [75]. The phase transition falls in the same universality class D as for vortex disorder [80], and one would expect the mechanism to be related in the same way to the appearance of Majorana zero-modes — even without any vortices to bind them. Can we demonstrate that in a computer simulation?

To address this question we use the spectral localizer approach pioneered by Loring and Schulz-Baldes [87, 88, 89, 90, 91, 92, 93, 94]. The spectral localizer embeds the Hamiltonian $\pm H$ on the diagonal of a 2×2 matrix, with the position operator $x \pm iy$ on the off-diagonal. Its spectrum quantifies whether Hamiltonian and position can be made commuting by a deformation that does not close the excitation gap [95, 96].

In a class D system the matrix signature of the spectral localizer (number of positive minus number of negative eigenvalues) identifies domains of different Chern number [90, 94]. As discussed by Volovik [97], the domain walls support low-lying states at energy $E \simeq \hbar v_{\mathrm{F}}/\ell$ for a domain of linear dimension ℓ. These states become Majorana zero-modes in the limit $\ell \to \infty$ of a percolating domain wall. By identifying the metal-insulator transition with the percolation transition of the domain walls we construct the phase diagram in a closed system, and compare with calculations based on the thermal conduction in an open system [75, 80].

4.2 Topological landscape function

4.2.1 Lattice Hamiltonian

The Bogoliubov-De Gennes Hamiltonian for a chiral p-wave superconductor is

$$H_{\mathrm{BdG}} = \begin{pmatrix} p^2/2m - E_{\mathrm{F}} & v_\Delta(p_x - ip_y) \\ v_\Delta(p_x + ip_y) & E_{\mathrm{F}} - p^2/2m \end{pmatrix}. \tag{4.1}$$

It acts on a two-component wave function $\Psi = (\psi_{\mathrm{e}}, \psi_{\mathrm{h}})$, the pair potential $\propto v_\Delta$ couples the electron and hole components (filled states above the Fermi level E_{F}, respectively, empty states below E_{F}, with $E_{\mathrm{F}} = \frac{1}{2} m v_{\mathrm{F}}^2$ in terms of the effective mass m and Fermi velocity v_{F}). Because this is equal-spin pairing, we can omit the spin degree of freedom.

The particle-hole symmetry relation,

$$\sigma_x H^*_{\mathrm{BdG}} \sigma_x = -H_{\mathrm{BdG}}, \tag{4.2}$$

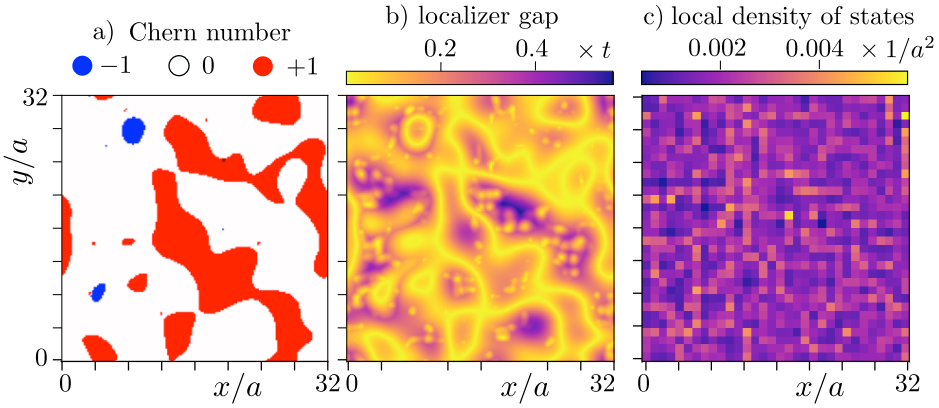

Figure 4.1. Panels a) and b) show the topological landscape function [Chern number $C(x, y)$ and localizer gap $\delta(x, y)$] in a disordered chiral p-wave superconductor (Hamiltonian (4.3), parameters $\Delta = 4t$, $\bar{\mu} = t$, $\delta\mu = 4\,t$, $L = 32a$, periodic boundary conditions). At these parameters the superconductor is in the thermal metal phase. Panel c) shows that the network of domain walls leaves no trace in the local density of states (integrated over the energy interval $|E| < 0.2\,t$).

places the system in symmetry class D [98]. Here σ_x is a Pauli matrix that acts on the electron-hole degree of freedom and the complex conjugation operation is taken in the real-space basis (so the momentum $\boldsymbol{p} = \hbar\boldsymbol{k} = -i\hbar\partial/\partial\boldsymbol{r}$ changes sign).

We discretize the Hamiltonian on a 2D square lattice (lattice constant a),

$$H = \begin{pmatrix} \varepsilon_k - \mu & \Delta(\sin ak_x - i \sin ak_y) \\ \Delta(\sin ak_x + i \sin ak_y) & \mu - \varepsilon_k \end{pmatrix},$$
$$\varepsilon_k = -t(\cos ak_x + \cos ak_y), \tag{4.3}$$

with the definitions $\Delta = (\hbar/a)v_\Delta$, $t = \hbar^2/ma^2$, $\mu = E_\mathrm{F} - 2t$.

We introduce electrostatic disorder by letting the chemical potential $\mu(x, y)$ fluctuate randomly, uniformly distributed in the interval $(\bar{\mu} - \delta\mu, \bar{\mu} + \delta\mu)$. Our approach requires some degree of smoothness of the fluctuating potential on the scale of the lattice constant, in what follows we choose the same μ on the four neighboring sites $(2n, 2m)$, $(2n + 1, 2m)$, $(2n, 2m + 1)$, and $(2n + 1, 2m + 1)$.

4.2.2 Spectral localizer: open boundary conditions

The spectral localizer for a two-dimensional class D Hamiltonian with open boundary conditions is [90]

$$\mathcal{L}(x_0, y_0) = \begin{pmatrix} H & 0 \\ 0 & -H \end{pmatrix} + \kappa\Omega(x - x_0, y - y_0), \tag{4.4a}$$

$$\Omega(x, y) = \begin{pmatrix} 0 & \sigma_0(x - iy) \\ \sigma_0(x + iy) & 0 \end{pmatrix}. \tag{4.4b}$$

The Hermitian operators $\mathcal{L}$ and Ω are both 4×4 matrices, we have introduced the 2×2 unit matrix σ_0 to indicate that Ω is diagonal in the electron-hole degree of freedom. Note also that x and y are operators (which do not commute with H), while x_0 and y_0 are parameters. Our choice $\kappa = 2.5\,t$ for the scale parameter κ is explained in App. 4.A.

The operator Ω breaks the $\pm E$ symmetry of the spectrum of $\mathcal{L}$, allowing for a nonzero matrix signature: Sig $\mathcal{L}$ = number of positive eigenvalues minus number of negative eigenvalues. This even integer determines a topological invariant, the Chern number [90],

$$C(x_0, y_0) = \tfrac{1}{2} \operatorname{Sig} \mathcal{L}(x_0, y_0), \tag{4.5}$$

of a domain containing the point (x_0, y_0). Domain walls, contours across which $C(x_0, y_0)$ changes by ± 1, are contours along which $\det\{\mathcal{L}\}(x_0, y_0)$ vanishes. These can be visualized by plotting the *localizer gap*

$$\delta(x_0, y_0) = \min_n |\lambda_n|, \quad \lambda_n \text{ eigenvalue of } \mathcal{L}(x_0, y_0), \tag{4.6}$$

which vanishes along the domain walls.

4.2.3 Spectral localizer: periodic boundary conditions

Our system is a square of size $L \times L$ in the x- and y-directions. To avoid edge states and focus on bulk properties, we prefer to work with periodic boundary conditions, rather than open boundary conditions. For that purpose, following Ref. [94], the term $x \pm iy$ on the off-diagonal of Ω is replaced by the periodic combination $\sin(2\pi x/L) \pm i \sin(2\pi y/L)$. The eigenvalues of $\Omega(x - x_0, y - y_0)$ then cannot distinguish between points x_0 and $x_0 + L/2$, or between y_0 and $y_0 + L/2$. To remove this doubling, cosine terms are added on the diagonal of Ω [94],

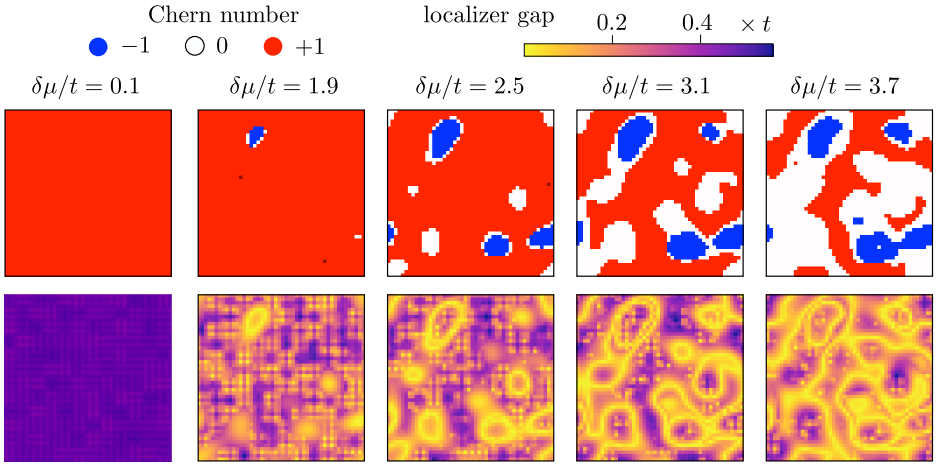

Figure 4.2. Topological landscape function (Chern number on top row, localizer gap on bottom row) for five different disorder strengths $\delta\mu$ at fixed $\bar{\mu} = 1.05\,t$ (and $\Delta = 4t$, $L = 24a$), to show the appearance of a percolating domain wall when $\delta\mu \gtrsim 3.1\,t$. These are results for a single realization of the random potential $\mu(x, y)$, only the amplitude is rescaled.

$$\mathcal{L}(x_0, y_0) = \begin{pmatrix} H & 0 \\ 0 & -H \end{pmatrix} + \kappa\Omega(x - x_0, y - y_0), \tag{4.7a}$$

$$\Omega(x, y) = \begin{pmatrix} \sigma_0[\cos(2\pi x/L) + \cos(2\pi y/L) - 2] & \sigma_0[\sin(2\pi x/L) - i\sin(2\pi y/L)] \\ \sigma_0[\sin(2\pi x/L) + i\sin(2\pi y/L)] & -\sigma_0[\cos(2\pi x/L) + \cos(2\pi y/L) - 2] \end{pmatrix}. \tag{4.7b}$$

For $|x|, |y| \ll L$ the localizers (4.4) and (4.7) coincide.

In Fig. 4.1 we show the resulting network of domain walls for a particular disorder realization (panels a and b). The topological information contained in the spectral localizer is essential: as shown in panel c, the domain walls do not show up in the local density of states near $E = 0$.

4.3 Phase diagram from percolation transition

4.3.1 Percolating domain walls

The clean system (without disorder, $\delta\mu = 0$) is a topologically trivial thermal insulator ($C = 0$) for $|\bar{\mu}| > 2t$ and a topologically nontrivial thermal insulator

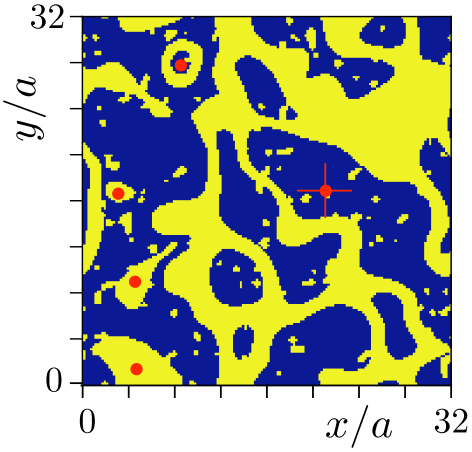

Figure 4.3. Same as Fig. 4.1b), but now the domain walls are highlighted in yellow, according to the criterion of localizer gap $\delta(\boldsymbol{r}) < 0.1\,t$. The location of the average $\bar{\boldsymbol{r}}$ ("center of mass") for each connected domain wall is indicated by a red dot. The extension ℓ of a domain wall is defined by $\ell^2 = 4\overline{|\boldsymbol{r} - \bar{\boldsymbol{r}}|^2}$. The red dot marked with a cross identifies the center of mass of a percolating domain wall ($\ell > L$).

($C = \pm 1$) for $|\bar{\mu}| < 2t$. At $\bar{\mu} = 0$ there is an insulator-to-insulator transition at which C changes sign [80]. Disorder introduces minority domains with a different Chern number than these clean values C_{clean}. See for example Fig. 4.1, where $\bar{\mu} = t$ and $C_{\text{clean}} = +1$.

The domain walls that separate regions of different Chern number support states close to the Fermi level, at energy $E \simeq \hbar v_{\text{F}}/\ell$ dictated by the requirement that the kinematic phase upon traveling once around the domain wall cancels the π Berry phase. When the extension ℓ of the largest domain wall reaches the system size L thermal conduction becomes possible near the Fermi level and the thermal insulator becomes a thermal metal. In Fig. 4.2 we show this percolation transition of topological domain walls for a single disorder realization, upon increasing the amplitude $\delta\mu$ of the potential fluctuations at fixed average $\bar{\mu}$.

To identify the percolation transition we need a computationally efficient way to measure the extension ℓ of a domain wall. We take localizer gap $\delta(x_0, y_0) < 0.1\,t$ as the criterion for a domain wall. All points $\boldsymbol{r} = (x_0, y_0)$ satisfying this criterion in a connected region belong to a single domain wall $\mathcal{D}$. We then compute the domain wall extension ℓ from the variance σ^2 of these points,

$$\ell = 2\sigma, \quad \sigma^2 = \overline{|\boldsymbol{r} - \bar{\boldsymbol{r}}|^2}, \tag{4.8}$$

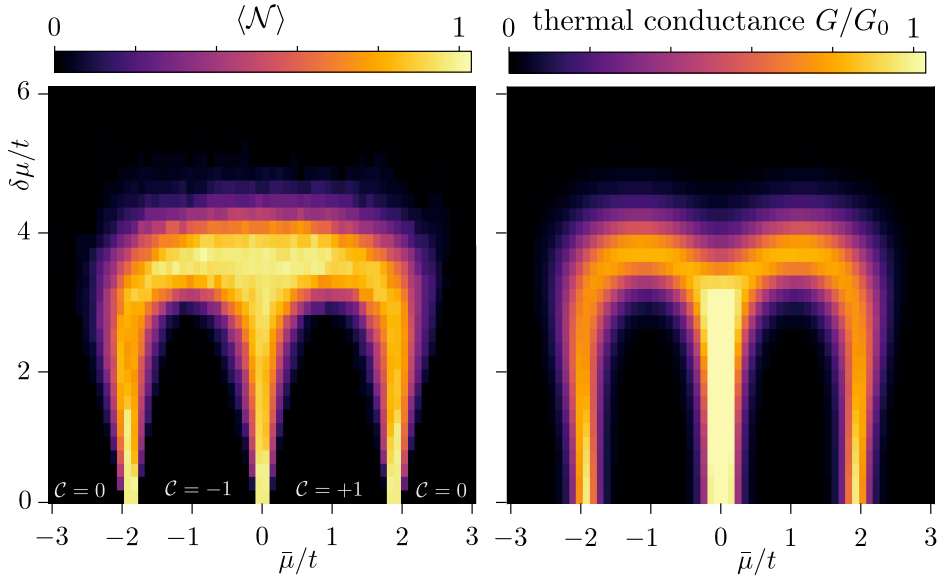

Figure 4.4. *Left panel:* Color scale plot of the average number $\langle \mathcal{N} \rangle$ of percolating domain walls, averaged over 100 disorder realizations in the chiral p-wave superconductor (parameters $\Delta = 4t$, $L = 24a$). The value of the Chern number C in the clean system ($\delta\mu = 0$) is indicated. *Right panel:* Dimensionless thermal conductance for the same system. The uniformly yellow bar at $\bar{\mu} = 0$ indicates $G/G_0 > 1$.

where $\overline{f(\boldsymbol{r})}$ averages a function $f(\boldsymbol{r})$ over all $\boldsymbol{r} \in \mathcal{D}$. The procedure is illustrated in Fig. 4.3. Our criterion for a *percolating* domain wall is $\ell > L$.

4.3.2 Phase diagram

The number $\mathcal{N}$ of percolating domain walls (with $\ell > L$) for a given disorder realization is averaged over the disorder. The resulting dependence of $\langle \mathcal{N} \rangle$ on the parameters $\bar{\mu}$ and $\delta\mu$ is shown in Fig. 4.4 (left panel). The region $\mathcal{N} \approx 1$ where the domain walls percolate is clearly distinguished.

The data in Fig. 4.4 is for a relatively small system ($L/a = 24$), in Fig. 4.5 we compare with a larger system. The critical disorder strength for the percolation transition is approximately scale invariant.

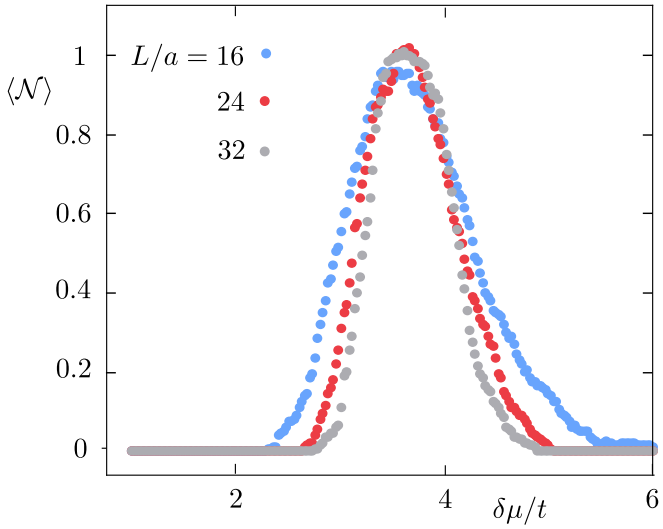

Figure 4.5. Comparison of the disorder strength dependence of the average number $\langle \mathcal{N} \rangle$ of percolating domain walls for different system sizes L. The data points are averaged over 200 disorder realizations (parameters $\Delta = 4t$, $\bar{\mu} = t$).

4.3.3 Comparison with thermal conductance

So far we have considered a closed system. If we connect leads at the two ends we can study the thermal conductance,

$$G = G_0 \, \mathrm{Tr}\, \boldsymbol{t}\boldsymbol{t}^\dagger, \quad G_0 = \pi^2 k_\mathrm{B}^2 T/6h, \tag{4.9}$$

at temperature T, with $\boldsymbol{t}$ the transmission matrix at the Fermi level. The result of such a calculation, using the KWANT code [99], is also shown in Fig. 4.4 (right panel).

If we compare with the percolation transition (left panel), we see a good quantitative agreement on the low-disorder side of the phase boundary. The high-disorder side misses a feature in the region near $\bar{\mu} = 0$, $\delta\mu = 4t$, where the thermal conductance localizes more quickly than inferred from the percolating domain walls. We are unsure about the origin of this difference. Apart from this region the agreement is quite satisfactory, without any adjustable parameters.

4.4 Conclusion

We have shown that the thermal metal phase in a model of a chiral p-wave superconductor with electrostatic disorder has a precursor in the thermally insulating phase: The disorder produces domain walls that separate topologically distinct regions (different Chern number). The thermal metal–insulator transition is accompanied by a percolation of the domain walls across the system, providing a transport channel for Majorana fermions (charge-neutral, low-energy excitations).

To reveal the network of domains walls we have used the matrix signature of the spectral localizer [90, 94]. We turned to this topological invariant after we were not able to identify localized Majorana fermions using a variation [100, 101] of the landscape function approach that has been so succesful in the study of Anderson localization [102, 103, 104, 105]. In a sense, the matrix signature of the spectral localizer functions as a *topological* landscape function, sensitive to topological electronic properties that remain hidden in the local density of states.

It would be interesting to study the critical exponent ν for the percolation transition of the topological domain walls (the exponent that governs the divergence of the largest domain size). Classical 2D percolation has $\nu_{\text{classical}} = 4/3$. It is suggestive that a recent numerical study [80] of the divergence of the localization length at the thermal metal–insulator transition found $\nu \approx 1.35$, but the proximity to $\nu_{\text{classical}}$ may well be accidental.

Data and code availability

Our computer codes are provided in a Zenodo repository [106].

Appendices

4.A Spectral localizer in a clean system

We have tested the ability of the spectral localizer (4.7) to identify the Chern number domains in a clean system, with a smoothly varying μ, where the boundaries are known analytically [80]:

$$C = \begin{cases} 0 & \text{if } \mu < -2t, \\ -1 & \text{if } -2t < \mu < 0, \\ +1 & \text{if } 0 < \mu < 2t, \\ 0 & \text{if } \mu > 2t. \end{cases} \tag{4.10}$$

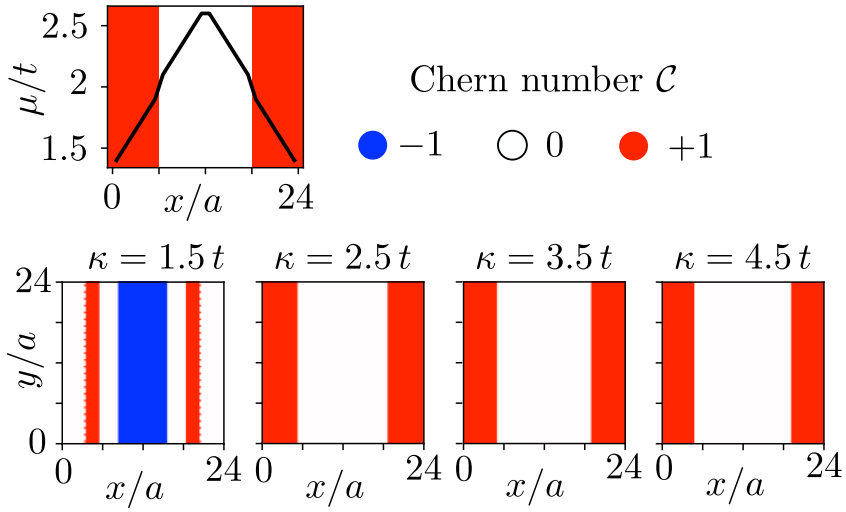

Figure 4.6. Top panel: linearly varying $\mu(x)$ (at constant $\Delta = 4t$), producing a central domain of Chern number $C = 0$, flanked by domains of $C = +1$. The domain walls are at $x/a = 6$ and $x/a = 12$. Bottom panels: Chern number domains produced by the spectral localizer, via Eq. (4.5), for different values of the scale parameter κ. We need $\kappa \gtrsim 2t$ for reliable results.

This test allows us to find a suitable value of the scale parameter κ.

Refs. [90, 94] argue that κ should be of the order of the norm of the Hamiltonian, which in our case is below $10^{-2}\,t$. We find a poor performance for such small κ, see Fig. 4.6, we need $\kappa \gtrsim 2t$ to reliably identify the domain walls. The results in the main text are for $\kappa = 2.5\,t$.